Using the Pauli Scattering Mechanisms for Analysis of Polarimetric SAR Images from RADARSAT Constellation and TanDEM-X Missions

Knut Eldhuset

***Abstract*—This article describes techniques for extraction of information in polarimetric images from RADARSAT constellation mission (RCM) and TanDEM-X (TDX) and TerraSAR-X (TSX) satellites. Using the boundary conditions of Maxwell's equations it is shown how the single bounce and double bounce scattering can be extracted from quad-pol and compact polarimetric (CP) SAR. We develop new equations to calculate the Pauli decomposition from simulated CP data using RCM quad-pol data. The RCM CP option is circular transmit, linear receive. We find that using quad-pol data performs better than using CP data for Pauli decomposition, especially extraction of the *HV* component. Estimation of single bounce and double bounce scattering from RCM CP data is feasible and yields more information about scattering properties than the CP components alone. We show how more information can be extracted from bistatic TSX/TDX quad-pol data by estimation of the coherence of the different Pauli components and optimization of the interferometric coherence using ships as detection objects. This is a unique opportunity to use optimized coherence on moving ships for characterizing their structure.**

***Index Terms*—Interferometric coherence, polarimetry, scattering mechanism, synthetic aperture radar (SAR).**

I. Introduction

THE Canadian RADARSAT constellation mission (RCM) was launched in June 2019 and consists of three satellites and followed the RADARSAT-1 and RADARSAT-2 satellites [1], [2]. The RCM is C-band and has a number of modes, many of them inherited from ancient satellites. For the first time a SAR compact polarimetry (dual-pol) option is available in space for most of the RCM modes. A number of papers have studied how a dual-pol SAR system may perform compared to a quad-pol SAR system. This is of great interest since the swath might be doubled without the need to double the PRF or double the average transmitted power [3], [4]. In [5], they proposed a concept where the radar transmits a linear polarized field at 45° (called $\pi/4$-mode) with respect to H and V orientations and receives coherently H and V components. In [6] and [7], they compared the $\pi/4$-mode and the circular transmit, linear receive (CTLR) mode where the SAR transmits a circular wave and receives on H and V (CH, CV). CTLR is the compact polarimetry mode implemented on RCM. A third method is the dual circular (right or left) transmission and right and left reception.

In the studies abovementioned they did two assumptions to reconstruct pseudo quad-pol data (see beginning of Section IV). In this article, we need only one of these assumptions (reflection symmetry) and develop new equations to reconstruct the absolute value of the pseudo Pauli components for the CTLR mode. We estimate the Pauli components from RCM quad-pol mode and compare with the pseudo Pauli components for the CTLR mode which are calculated from quad-pol data. In the literature formulas for calculation of double bounce and single bounce scattering are mostly given without explaining the principle or deriving the formulas. Here, we start with the boundary conditions of Maxwell's equations to show how the double bounce and single bounce scattering can be understood by illustrating the reflections of the radar waves with polarimetric field vectors for the quad-pol and the CTLR modes.

The primary objective of the TanDEM-X mission (X-band) was to generate a global digital elevation model (DEM) [8], a High Resolution DEM with 12 m horizontal resolution. In addition, the system was reconfigurable with several other modes such as the staring spotlight mode with resolution better than 1 m. In [9], we focused on generation and estimation of the height accuracy of geocoded DEMs and in [10], the data were used for change detection using time and look angle series of geocoded staring spotlight images. Among several interferometric modes we have in this article selected the bistatic mode and the quad-pol option. Due to the very small time difference between TerraSAR-X (TSX) and TanDEM-X (TDX), it is possible to achieve good coherence over moving ships. Indeed, TDX/TSX was the first single-pass quad-pol radar interferometer in space [8]. We estimate the coherence of the different components in the Pauli decomposition and finally do an optimization of the coherence.

The main objective in this article is to illustrate the role of the Pauli scattering components in different polarimetry and polarimetric interferometry SAR (PolInSAR) applications. By using the Pauli decomposition we shall compare quad-pol and compact polarimetry (CP) using RCM data. We shall use data from TDX/TSX to combine polarimetry and interferometry with application to ship detection. In Section II, the modes and the

Manuscript received 23 March 2022; revised 25 May 2022 and 22 June 2022; accepted 6 July 2022. Date of publication 13 July 2022; date of current version 27 July 2022. This work was supported by the project "Satellites in the Defence 2017–2024" and financed by the Norwegian Defence Research Establishment (FFI).

The author is with the Department of Sensor and Surveillance Systems, Norwegian Defence Research Establishment (FFI), 2007 Kjeller, Norway (e-mail: knut.eldhuset@ffi.no).

Digital Object Identifier 10.1109/JSTARS.2022.3190311

data we use are briefly described. In Section III, we use the electrodynamic equations for polarimetric SAR waves to show how we extract the Pauli double bounce and single bounce scattering components from quad-pol and CP SAR data. This should be a contribution to the literature to better understand the physical scattering mechanisms. In Section IV, we develop new equations for direct extraction of pseudo Pauli components from pseudo CP SAR without estimation of each pseudo quad-pol component. In [5] and [7], they first estimate the pseudo quad-pol components. Therefore, they have to solve one more equation and use one more constraint than we need in our method. In Section V, we review very briefly a method known from the literature for optimization of coherence using PolInSAR data. The review is provided in order to show how the Pauli components are used in the algorithm and how they are needed to define the expression for complex coherence. We demonstrate this technique by analysis of moving ships in bistatic TDX/TSX PolInSAR data with images with very short time separation. Section VI describes how RCM quad-pol and CP data, and TSX/TDX PolInSAR data are used to apply the abovementioned techniques and try to evaluate their performance.

II. TDX/TSX and RCM Modes and Data Sets

A. TDX/TSX and RCM Modes

The single look complex (SLC) data from RCM we could freely download from a Canadian government site [11]. An overview and status of the RCM satellites can be found in [1] and how to get access to data, see [2].

We received TDX/TSX Coregistered Single-look Slant range Complex (CoSSC) data in quad polarization as science user from German Aerospace Center (DLR) under an Announcement of Opportunity project (AO-projectNTI_INS6664). The science phase started in October 2014 and was completed in December 2015. Within this time, two main interferometric operation modes were executed: the pursuit monostatic mode (October 2014–February 2015) and the bistatic mode (March 2015–December 2015). In the bistatic mode, the along-track distance was mostly less than 500 m and either TSX or TDX was used as a transmitter and both satellites received the scattered echo. In this article, we only study the images from the bistatic mode. For further details on the modes and science phase timeline, see [12]. The processing of CoSSC products has been described in [13].

B. Data Set

The datasets we have analyzed in this article are listed in Table I. The first dataset is a quad-pol RCM-3 image over Quebec in Canada and the second one is a compact polarimetry (CTLR) image over Winnipeg in Canada. The third image is a TDX/TSX interferometric quad-pol pair in bistatic strip map mode, which we received in the AO-project mentioned previously. For this interferometric image pair the along-track distance between TSX and TDX is only 201 m (0.027 s temporal separation) and the area is around Gibraltar.

TABLE I
Descending Right-Looking SLC Scenes

	Date	Pixel size (m) (az,ra)	Inc(°)	Polarization
RCM-3 strip	December 29 2019	3.3 3.1	27.0	HH HV VH VV
RCM-1 strip	February 19 2020	2.2 1.4	41.0	CH CV
TDX/TSX bistatic strip	November 22 2015	2.2 0.9	32.7	HH HV VH VV

SLC scenes, which were studied in this article. The pixel size is given for azimuth (az) and slant range (ra). The incidence angle (Inc) is in the middle of the scenes. The pass direction for all scenes is descending. The three scenes are over Quebec, Winnipeg and Gibraltar, respectively. The height of ambiguity is 111.5 m for the TDX/TSX image pair.

III. Derivation of Scattering Amplitudes From Electrodynamic Equations

The single or odd-bounce scattering and double or even-bounce scattering components in the Pauli decomposition are usually derived by decomposing the scattering matrix as on p. 214 in [14]. This is a simple technical trick and does not give an understanding of the physical mechanisms. To better understand these mechanisms, one can use the laws governing reflection and refraction of polarized electromagnetic waves. These laws can be derived by using boundary conditions of the Maxwell's equations and can be found in Chapter 9 and 7.65 in Chapter 7 in textbook [15]. In this book single bounce at oblique and normal incidence is considered. Here, we shall consider single scattering and double scattering at oblique incidence, which are components in the Pauli decomposition. Single scattering means that the wave is reflected without doing multiple bounces as if it hit a facet normal to the direction of the incident wave. Such facets will cause scattering from waves on the ocean or from slightly rough surfaces on fields. We assume that the boundary is a perfect conducting surface, hence, we consider a totally reflected wave.

A. Single Bounce Scattering

Suppose the *xy* plane and the *yz* plane form the boundary between the two media. $\hat{x}$, $\hat{y}$, and $\hat{z}$ are the unit vectors for the coordinate axes shown in Fig. 1. Then, we define the unit propagation (or wave) vectors for incident wave $\hat{k}_I$ and single bounce (direct reflection) $\hat{k}_R$

$$\hat{k}_I = \hat{z} \tag{1}$$

$$\hat{k}_R = -\hat{z} \tag{2}$$

and the unit vector for vertical polarization is defined by

$$\hat{v} = \hat{x}\ . \tag{3}$$

Now, we consider single bounce scattering for an incident and reflected vertical electrical field at normal incidence. The incident $\vec{E}_I$ and reflected $\vec{E}_R$ electric fields are illustrated in

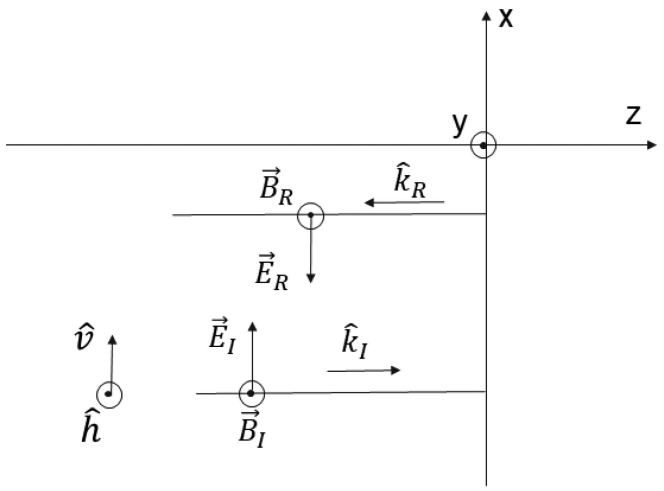

Fig. 1. Single bounce scattering at normal incidence for an incident vertical polarized electric field, which is parallel to the plane of incidence (*xz* plane), *VV* scattering.

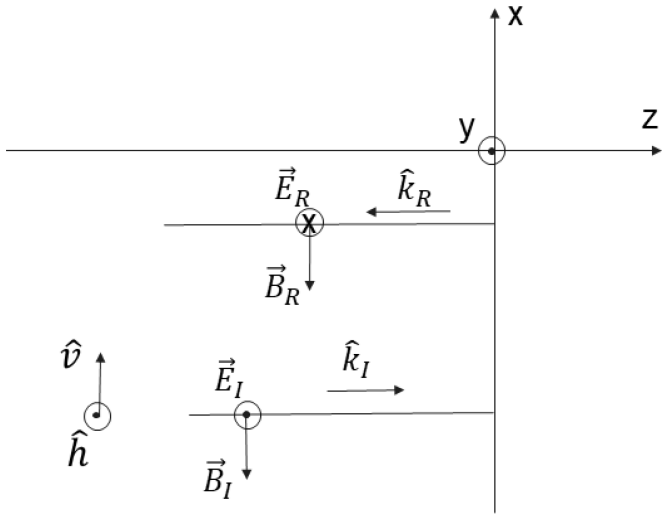

Fig. 2. Single bounce scattering at normal incidence for an incident horizontal polarized electric field, which is perpendicular to the plane of incidence (*xz* plane), *HH* scattering.

Fig. 1 and given by

$$\vec{E}_I = \tilde{E}_{I0}\ \hat{v}\ e^{i[k\ z-\omega\ t]} \tag{4}$$

$$\vec{E}_R = \tilde{E}_{R0}\ \ (-\hat{v}\ )\ e^{i[-k\ z-\omega\ t]} \tag{5}$$

where $\tilde{E}_{I0}$ and $\tilde{E}_{R0}$ are the complex amplitudes and i is the imaginary unit. The wave number k is defined by

$$k\ =\ \omega\sqrt{\mu_0\ \varepsilon_0} \tag{6}$$

where ω is the angular frequency of the wave, μ_0 is the permeability, and ε_0 is the permittivity in free space. Then, we consider the single bounce scattering illustrated in Fig. 2 for an incident and reflected horizontal electrical field at normal incidence

$$\vec{E}_I = \tilde{E}_{I0}\ \hat{h}\ e^{i[k\ z-\omega\ t]} \tag{7}$$

$$\vec{E}_R = \tilde{E}_{R0}\ \ \left(-\hat{h}\ \right)\ e^{i[-k\ z-\omega\ t]} \tag{8}$$

where the unit vector for horizontal polarization is defined by

$$\hat{h} = \hat{y}\ . \tag{9}$$

The corresponding magnetic fields, the incident $\vec{B}_I$ and the reflected $\vec{B}_R$ are given by the cross products

$$\vec{B}_I = \frac{1}{c}\ \hat{k}_I \times \vec{E}_I \tag{10}$$

$$\vec{B}_R = \frac{1}{c}\ \hat{k}_R \times \vec{E}_R \tag{11}$$

where c is the speed of light. Using (5) and (8) and remember that $e^{i\pi}\ =\ -1$, we can write the reflected fields $\vec{E}_R^{VV}$ for vertical polarization and $\vec{E}_R^{HH}$ for horizontal polarization

$$\vec{E}_R^{VV}\ = \tilde{E}_{R0}\ \hat{v}\ e^{i\ (\pi-\varphi_I-\omega t)=}\ \ S_{VV}\ \hat{v} \tag{12}$$

$$\vec{E}_R^{HH}\ = \tilde{E}_{R0}\ \hat{h}\ e^{i\ (\pi-\varphi_I-\omega t)}\ \ = S_{HH}\ \ \hat{h} \tag{13}$$

where we have defined the complex scattering amplitudes S_{VV} and S_{HH}. Since the phase is the same in the two exponentials, we see that the complex sum of S_{HH} and S_{VV} yields maximum response in the case of single bounce scattering

$$S_{SB} = S_{VV} + S_{HH} \tag{14}$$

S_{SB} is the single or odd-bounce scattering component in the Pauli decomposition [see (43)]. It is also called surface scattering since this is the dominating scattering from large areas like ocean or fields.

B. Double Bounce Scattering

Now, we define the unit propagation (or wave) vectors for incident $\hat{k}_I$, single bounce (first reflection) $\hat{k}_{R1}$, and double bounce scattering (double reflection) $\hat{k}_{R2}$

$$\hat{k}_I\ =\ (\sin(\theta)\ ,\ 0, \cos(\theta)) \tag{15}$$

$$\hat{k}_{R1}\ =\ (\sin(\theta)\ ,\ 0, -\cos(\theta)) \tag{16}$$

$$\hat{k}_{R2}\ =\ (-\sin(\theta),\ 0, -\cos(\theta)) \tag{17}$$

where θ is the angle of incidence and the unit vector for vertical polarization is defined by

$$\hat{v} = \cos(\theta)\ \ \hat{x} - \sin(\theta)\ \ \hat{z} \tag{18}$$

where $\hat{x}$ and $\hat{z}$ are the unit vectors for the coordinate axes.

The incident $\vec{E}_I$, first reflected $\vec{E}_{R1}$, and double reflected $\vec{E}_{R2}$ electric fields are illustrated in Fig. 3 and given by

$$\vec{E}_I = \tilde{E}_{I0}\ \ (\cos(\theta)\,\hat{x} - \sin(\theta)\ \ \hat{z})\ \ e^{i[k(\sin(\theta)\ \mathrm{x}+\cos(\theta)\ z)-\omega t]} \tag{19}$$

$$\vec{E}_{R1} = \tilde{E}_{R10}(-\cos(\theta)\,\hat{x} - \sin(\theta)\ \ \hat{z})\ \ e^{i[k(\sin(\theta)\ \mathrm{x}\ -\cos(\theta)\ z)-\omega t]} \tag{20}$$

$$\vec{E}_{R2} = \tilde{E}_{R20}(-\cos(\theta)\,\hat{x} + \sin(\theta)\ \ \hat{z})\ \ e^{i[k(-\sin(\theta)\ \mathrm{x}\ -\cos(\theta)\ z)-\omega t]} \tag{21}$$

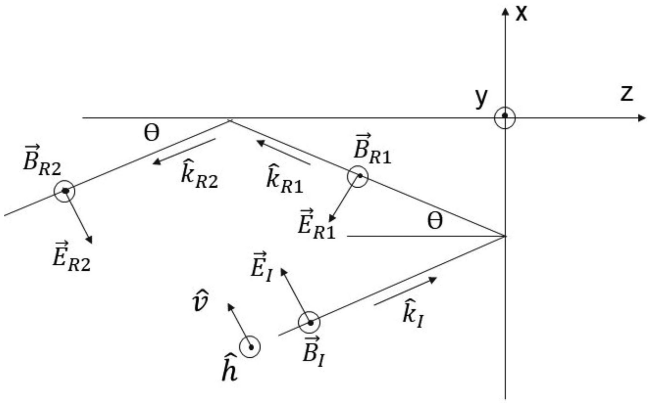

Fig. 3. Double bounce scattering for an incident wave, which is parallel to the plane of incidence (*xz* plane), *VV* scattering.

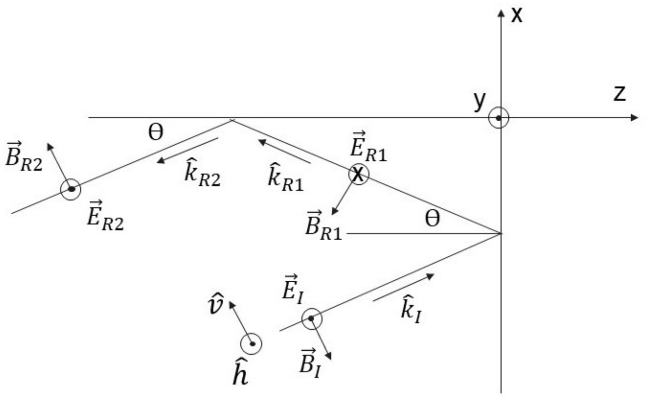

Fig. 4. Double bounce scattering for an incident wave, which is perpendicular to the plane of incidence (*xz* plane), *HH* scattering.

where $\tilde{E}_{I0}$, $\tilde{E}_{R10}$, and $\tilde{E}_{R20}$ are complex amplitudes and i is the imaginary unit. The wavenumber k was defined in (6). The corresponding magnetic fields, the incident $\vec{B}_I$, first reflected $\vec{B}_{R1}$, and double reflected $\vec{B}_{R2}$ are given by the cross products

$$\vec{B}_I = \frac{1}{c}\,\hat{k}_I \times \vec{E}_I \tag{22}$$

$$\vec{B}_{R1} = \frac{1}{c}\,\hat{k}_{R1} \times \vec{E}_{R1} \tag{23}$$

$$\vec{B}_{R2} = \frac{1}{c}\,\hat{k}_{R2} \times \vec{E}_{R2}\,. \tag{24}$$

For vertical polarization, we write the incident and double reflected waves more compactly as

$$\vec{E}_I = \tilde{E}_{I0}\,\hat{v}\,e^{i\,(\varphi_I - \omega t)} \tag{25}$$

$$\vec{E}_{R2} = \tilde{E}_{R20}\;(-\hat{v})\;e^{i\,(-\varphi_I - \omega t)} \tag{26}$$

$$\varphi_I = \;k\,(\sin(\theta)\;\mathrm{x} + \cos(\theta)\;z)\,. \tag{27}$$

We remember that $e^{i\pi} = \,-1$ and write (26) as

$$\vec{E}_{R2} = \tilde{E}_{R20}\,\hat{v}\,e^{i\,(\pi - \varphi_I - \omega t)}. \tag{28}$$

The horizontal polarization vector was defined in (9) $\hat{h} = \hat{y}$. The incident, first reflected and double reflected electric fields are illustrated in Fig. 4 and given by

$$\vec{E}_I = \tilde{E}_{I0}\;\;\widehat{y}\;\;e^{i[k(\sin(\theta)\;\mathrm{x} + \cos(\theta)\;z) - \omega t]} \tag{29}$$

$$\vec{E}_{R1} = \tilde{E}_{R10}\;\;\widehat{y}\;\;e^{i[k(\sin(\theta)\;\mathrm{x}\;-\;\cos(\theta)\;z) - \omega t]} \tag{30}$$

$$\vec{E}_{R2} = \tilde{E}_{R20}\;\;\widehat{y}\;\;e^{i[k(-\sin(\theta)\;\mathrm{x}\;-\;\cos(\theta)\;z) - \omega t]}. \tag{31}$$

The magnetic fields are written in the same way as (22)–(24). We simplify (29) and (31) and replace $\widehat{y}$ by $\widehat{h}$

$$\vec{E}_I = \tilde{E}_{I0}\,\hat{h}\,e^{i\,(\varphi_I - \omega t)} \tag{32}$$

$$\vec{E}_{R2} = \tilde{E}_{R20}\,\hat{h}\,e^{i\,(-\varphi_I\;-\omega t\;)}. \tag{33}$$

Then, we use (28) and write the double reflected electric field and adding the super- and subscript *VV*

$$\vec{E}^{VV}_{R2} = \tilde{E}_{R20}\,\hat{v}\,e^{i\,(\pi - \varphi_I - \omega t)} \;= \tilde{E}_{I0}\,S'_{VV}e^{i\pi}\,\hat{v} \tag{34}$$

where the scattering amplitude S'_{VV} does not contain the phase π. We rewrite (33) and (34) and define the double reflected fields $\vec{E}^{HH}_{R2}$ for horizontal and $\vec{E}^{VV}_{R2}$ for vertical polarization

$$\vec{E}^{HH}_{R2} = \tilde{E}_{I0}S_{HH}\,\hat{h} \tag{35}$$

$$\vec{E}^{VV}_{R2} = \tilde{E}_{I0}\,S_{VV}\,\hat{v} \tag{36}$$

where we have defined the complex scattering amplitudes S_{HH} and S_{VV}. S_{VV} includes the phase π. The phase $\varphi_I - \omega t$ is the same in (33) and (34), hence, the phase difference is π in the complex scattering amplitudes in (35) and (36). Therefore, we have to take the complex difference to obtain maximum response

$$S_{DB} = S_{VV}\; - S_{HH} \tag{37}$$

S_{DB} is the double or even-bounce scattering component in the Pauli decomposition [see (43)].

C. Single Bounce and Double Bounce Scattering for Circularly Polarized Fields

We shall derive the formula for detecting double bounce and single bounce scattering for circular transmitted and linear (horizontal and vertical) received polarization. If we write the circularly double reflected electric field as the sum of (33) and (28) with $\pi/2$ phase difference we get

$$\vec{E}_{R2} = \tilde{E}_{R20}\,\hat{h}\,e^{i\,(-\varphi_I - \omega t - \pi/2)} + \tilde{E}_{R20}\hat{v}\,e^{i\,(\pi - \varphi_I - \omega t)}\,. \tag{38}$$

If we assume that the vertical receiver cancels the $\pi/2$ phase, the detected signal in the horizontal receiver $\vec{E}_{CH}$ is

$$\vec{E}_{CH} = \tilde{E}_{R20}\hat{h}\,e^{i\,(-\varphi_I - \omega t)} \;= \hat{h}\;\;\tilde{E}_I\,S_{CH} \tag{39}$$

and the detected signal in the vertical receiver $\vec{E}_{CV}$

$$\vec{E}_{CV} = \;\tilde{E}_{R20}\hat{v}\,e^{i\,(\pi - \varphi_I - \omega t)} \;= \;\hat{v}\,\tilde{E}_I e^{i\pi}\;\;S'_{CV} = \hat{v}\;\;\tilde{E}_i S_{CV} \tag{40}$$

where we have defined the complex scattering amplitudes S_{CH} and S_{CV}. Due to the phase difference π we detect a double

bounce (S_{CDB}) reflected circular wave by taking the difference of the complex scattering amplitudes in (39) and (40)

$$S_{\text{CDB}} = S_{CV} \; - S_{CH} \tag{41}$$

which gives maximum response. In the same way, as we derived (14), we detect single bounce scattering S_{CSB} from the linear detected circularly wave

$$S_{\text{CSB}} = S_{CV} \; + S_{CH} \tag{42}$$

which gives maximum response.

IV. Pseudo Pauli Decomposition of CTLR Mode Data

A quad-pol SAR system alternatively transmits two orthogonally polarized pulses and receives the returns in two orthogonal polarizations. Then, we can use the complex scattering amplitudes S_{HH}, S_{HV} , and S_{VV} to define the Pauli scattering vector $\vec{k}_{\text{PAULI}}$ ([14] p. 65 and [16] p. 47)

$$\vec{k}_{\text{PAULI}} = \frac{1}{\sqrt{2}} \left[S_{HH} + S_{VV} \; S_{VV} - S_{HH} 2 S_{HV} \right]^T \tag{43}$$

where scattering reciprocity is assumed: $S_{HV} = S_{VH}$. The first component is single bounce scattering given in (14), the second component is double bounce scattering given in (37). Here, we shall calculate the absolute value of the Pauli components in (43) for the CTLR mode. We do the same assumption of reflection symmetry as they did in [7] where they assume that the co-pol/cross-pol correlations are zero: $S_{HH} \; S_{HV}^* = \; 0$ and $S_{VV} \; S_{HV}^* = \; 0$. However, we do not try to reconstruct the quad-pol covariance matrix, hence, we do not need the constraint introduced in [5], which they also used in [7].

Now, we show how the absolute value of the pseudo Pauli components $|S_{DB}|_{PQ} = |S_{VV} - S_{HH}|$, $|S_{SB}|_{PQ} = |S_{HH} + S_{VV}|$, and $|S_{HV}|_{PQ}$ can be reconstructed from circular transmitted polarization and dual linear receive polarization also called hybridpolarity architecture [3]. Using the scattering matrix and assuming $S_{VH} = S_{HV}$, we can write the received signal for the CTLR mode

$$\begin{bmatrix} S_{RH} \\ S_{RV} \end{bmatrix} = \begin{bmatrix} S_{HH} & S_{HV} \\ S_{HV} & S_{VV} \end{bmatrix} \begin{bmatrix} 1 \\ -i \end{bmatrix} \tag{44}$$

where S_{RH} is the scattering amplitude for right circular transmit-linear horizontal receive and S_{RV} is the scattering amplitude for right circular transmit-linear vertical receive. The unit vector $\frac{1}{\sqrt{2}}\left[\begin{smallmatrix} 1 \\ -i \end{smallmatrix}\right]$ is the right-handed Jones vector [14] (p. 38) and the imaginary unit i in (44) indicates that the phase difference of the horizontal and vertical transmitted electric field components is $\pi/2$, which means right-handed circular polarization. The scattering vector for the CTLR mode $\vec{k}_{\text{CTLR}}$ is defined by [6]

$$\vec{k}_{\text{CTLR}} = \frac{1}{\sqrt{2}} [S_{RH} S_{RV}]^T \tag{45}$$

$$S_{RH} = (S_{HH} \; - i S_{HV}) \tag{46}$$

$$S_{RV} = \; (S_{HV} - i S_{VV}) \; . \tag{47}$$

The covariance matrix for the CTLR mode is given by

$$[C_{\text{CTLR}}] = \begin{bmatrix} C_{11} & C_{12} \\ C_{21} & C_{22} \end{bmatrix} = \frac{1}{2} \left\langle \begin{bmatrix} |S_{RH}|^2 & S_{RH} S_{RV}^* \\ S_{RH}^* S_{RV} & |S_{RV}|^2 \end{bmatrix} \right\rangle \tag{48}$$

$$C_{11} = \frac{1}{2} \left(\langle |S_{HH}| \rangle^2 + \langle |S_{HV}| \rangle^2 \right) \tag{49}$$

$$C_{12} = \frac{1}{2} \left(i \langle S_{HH} S_{VV}^* \rangle - i \langle |S_{HV}| \rangle^2 \right) \tag{50}$$

$$C_{21} = \frac{1}{2} \left(-i \langle S_{HH}^* S_{VV} \rangle + i \langle |S_{HV}| \rangle^2 \right) \tag{51}$$

$$C_{22} = \frac{1}{2} \left(\langle |S_{VV}| \rangle^2 + \langle |S_{HV}| \rangle^2 \right) \tag{52}$$

where $\langle \cdot \cdot \rangle$ indicates spatial ensemble averaging, which was implemented here by taking the complex average in 3×3 windows. The elements C_{nm} in (49)–(52) are calculated using (46)–(48) and assuming reflection symmetry, which means that the co-pol/cross-pol correlations are zero ([6]): $\langle S_{HH} \; S_{HV}^* \rangle = \; 0$ and $\langle S_{VV} \; S_{HV}^* \rangle = \; 0$. Using (51) and (52) and taking the product of (49) and (50) and solving for $|S_{HV}|^2$, the pseudo quad-pol cross-polarization component $|S_{HV}|_{PQ}$ can be reconstructed by

$$|S_{HV}|_{PQ}^2 = \frac{C_{1R}}{C_{2R}} \tag{53}$$

where

$$C_{1R} = \; 4 \left(-C_{11} C_{22} + C_{12} C_{21} \right) \tag{54}$$

$$C_{2R} = \; 2 \left(-C_{11} - C_{22} + i C_{12} - i C_{21} \right) . \tag{55}$$

Having in mind that

$$|S_{SB}|^2 = (S_{HH} + S_{VV}) \; (S_{HH} + S_{VV})^* \tag{56}$$

and using (49)–(52) we can estimate the square of the pseudo quad-pol single bounce component $|S_{SB}|_{PQ}^2$

$$|S_{SB}|_{PQ}^2 \; = 2 \left(C_{11} + C_{22} - i C_{12} + i C_{21} \right) . \tag{57}$$

Also remember that

$$|S_{DB}|^2 = (S_{VV} - S_{HH}) \; (S_{VV} - S_{HH})^* \tag{58}$$

and using (49)–(52) we can estimate the square of the pseudo quad-pol double bounce component $|S_{DB}|_{PQ}^2$

$$|S_{DB}|_{PQ}^2 \; = 2 \left(C_{11} + C_{22} + i C_{12} - i C_{21} \right) - 4 \, |S_{HV}|_{PQ}^2 . \tag{59}$$

The elements C_{nm} in (49)–(52) are estimated from the real quad-pol data: S_{HH}, S_{HV}, S_{VH}, and S_{VV}.

V. Optimizing Coherence Using the Pauli Components

A detailed description of a method for optimizing coherence can be found in [14] or [16]. Since this description is quite lengthy, we only sketch the main principles in order to show how the Pauli components are used to derive the expression for interferometric coherence in (67). If we have two satellites with short time separation with fully polarimetric radar system we can generate coherence image between each of the polarization

channels or we can also generate coherence image from the Pauli components

$$S_{1_{DB}} = S_{1_{VV}} - S_{1_{HH}} \tag{60}$$

$$S_{2_{DB}} = S_{2_{VV}} - S_{2_{HH}} \tag{61}$$

$$S_{1_{SB}} = S_{1_{VV}} + S_{1_{HH}} \tag{62}$$

$$S_{2_{SB}} = S_{2_{VV}} + S_{2_{HH}}. \tag{63}$$

Equation (60) and (61) can be used to estimate the double bounce images for satellite no 1 (TSX) and no 2 (TDX) and then generate the coherence image from $S_{1_{DB}}$ and $S_{2_{DB}}$. The same can be done for single bounce images using (62) and (63). To optimize the coherence we start with calculation of the Pauli scattering vectors $\vec{k}_1$ and $\vec{k}_2$ of satellite no 1 (TSX) and satellite no 2 (TDX)

$$\vec{k}_1 = \frac{1}{\sqrt{2}} \left[S_{1_{SB}}, S_{1_{DB}}, 2S_{1_{HV}} \right]^T \tag{64}$$

$$\vec{k}_2 = \frac{1}{\sqrt{2}} \left[S_{2_{SB}}, S_{2_{DB}}, 2S_{2_{HV}} \right]^T. \tag{65}$$

Then, we maximize the complex Lagrangian L

$$L = \vec{w}_1^{\dagger} \left[\Omega_{12}\right] \vec{w}_2 + \lambda_1 \left(\vec{w}_1^{\dagger} \left[T_{11}\right] \vec{w}_1 - C_1 \right) + \lambda_2 \left(\vec{w}_2^{\dagger} \left[T_{22}\right] \vec{w}_2 - C_2 \right) \tag{66}$$

where $\vec{w}_1$ and $\vec{w}_2$ are considered as generalized scattering mechanisms. † is the Hermitian adjoint operation. If $\vec{w}_1 = [1, 0, 0]$, the scattering mechanism is single bounce for satellite no 1 since $\vec{k}_1$ in (58) is the projection onto the vector $\vec{w}_1$. C_1 and C_2 are constants, λ_1 and λ_2 are Lagrange multipliers. This maximizes the interferometric coherence γ

$$\gamma = \frac{\left\langle \vec{w}_1^{\dagger} \left[\Omega_{12}\right] \vec{w}_2 \right\rangle}{\sqrt{\left\langle \vec{w}_1^{\dagger} \left[T_{11}\right] \vec{w}_1 \right\rangle \left\langle \vec{w}_2^{\dagger} \left[T_{22}\right] \vec{w}_2 \right\rangle}}. \tag{67}$$

The Hermitian coherency matrices $[T_{11}]$, $[T_{22}]$ and the non-Hermitian matrix $[\Omega_{12}]$ are defined by

$$[T_{11}] = \left\langle \vec{k}_1 \cdot \vec{k}_1^{\dagger} \right\rangle \tag{68}$$

$$[T_{22}] = \left\langle \vec{k}_2 \cdot \vec{k}_2^{\dagger} \right\rangle \tag{69}$$

$$[\Omega_{12}] = \left\langle \vec{k}_1 \cdot \vec{k}_2^{\dagger} \right\rangle \tag{70}$$

where $\langle \cdot\cdot \rangle$ indicates spatial ensemble averaging. $[\Omega_{12}]$ contains both polarimetric and interferometric correlation information between $\vec{k}_1$ and $\vec{k}_2$. It turns out that we get three pairs of optimum scattering mechanism vectors $\vec{w}_{1opt}$ and $\vec{w}_{2opt}$ that are eigenvectors of the maximization above and the corresponding optimal coherence values γ_{opt_1}, γ_{opt_2}, and γ_{opt_3} are square root of the eigenvalues. The software for optimization of coherence was developed at the Norwegian Defence Research Establishment (FFI).

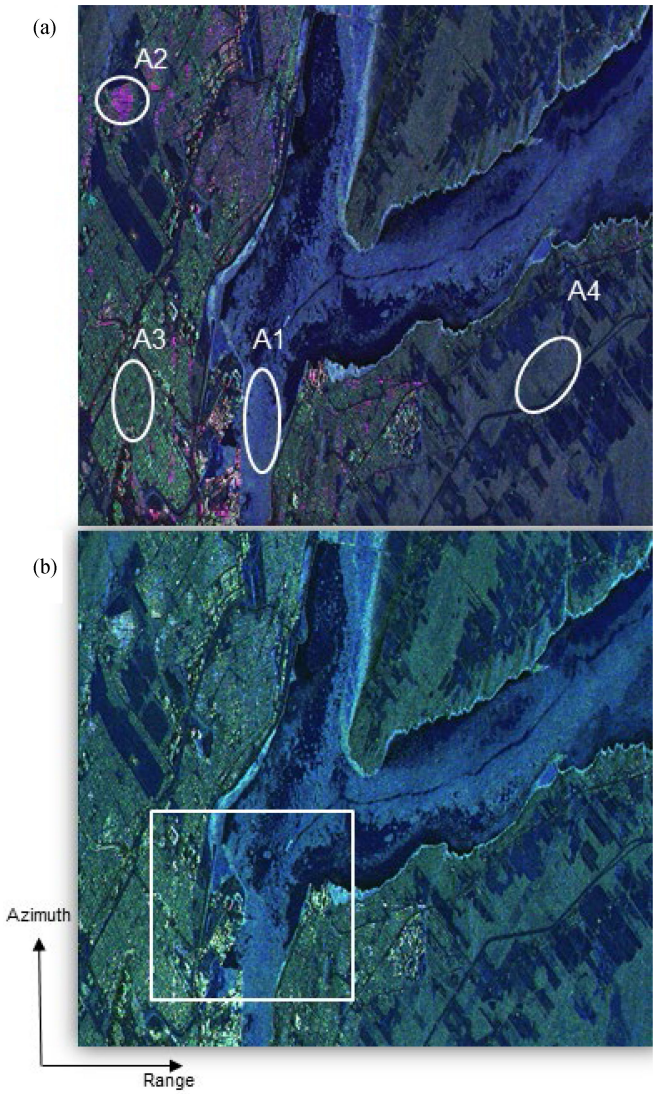

Fig. 5. RGB (Double bounce, 3·|*HV*|, single bounce) color composite of Pauli decomposition over Quebec, December 29, 2019. 2 × 2 averaged from azimuth pixel spacing = 3.3 m and ground range pixel spacing = 3.1 m. (a) RCM quad-pol. The subset areas A1, A2, A3, and A4 are used for estimation of ratio of pseudo quad-pol Pauli components in (b) and quad-pol Pauli components in (a). (b) CTLR simulation. The rectangle defines the area for the images in Fig. 6(a) and (b).

VI. Analysis of Polarimetric Images

A. Simulation of Pseudo Pauli Components From RCM Quad-Pol

The scattering vector in (43) contains the components of a Pauli decomposition. Fig. 5(a) shows an RGB color composite (2 × 2) of a Pauli decomposition of an RCM quad-pol image over the St. Lawrence river and Quebec in Canada. The urban areas typically appears as double bounce scattering (red), but also cross-polarization (*HV*) scattering (green). The water surface in the river and the fields in the right part of the image are mostly blue colored due to surface scattering. The ship in the middle of the image is mostly bright, which indicates much of all components. The front of the ship is red, which indicates double bounce scattering.

TABLE II
AMPLITUDES OF PSEUDO QUAD-POL PAULI COMPONENTS IN FIG. 6 AND QUAD-POL PAULI COMPONENTS IN FIG. 5 AND THEIR RATIOS

	Full scene	A1	A2	A3	A4
R_{SB}	1.10	1.09	1.14	1.10	1.09
$\lvert S_{SB}\rvert$	898	1418	2034	818	928
$\lvert S_{SB}\rvert_{PQ}$	989	1545	2318	903	1013
R_{DB}	0.80	0.71	0.73	0.88	0.77
$\lvert S_{DB}\rvert$	452	565	1623	508	513
$\lvert S_{DB}\rvert_{PQ}$	360	401	1181	446	395
R_{HV}	1.36	1.28	3.81	1.17	1.35
$\lvert S_{HV}\rvert$	196	272	189	286	225
$\lvert S_{HV}\rvert_{PQ}$	266	349	721	335	304

If the ratio is unity, it means that the pseudo quad-pol Pauli component and the quad-pol Pauli component is equal. The subset areas A1–A4 are shown in Fig. 5(a).

Fig. 5(b) shows an RGB color composite (2×2) of the pseudo Pauli components given by (59), (53), and (57) of a CTLR simulated image using the same quad-pol data as in Fig. 5(a). We define the ratio of the absolute values of the pseudo quad-pol Pauli components defined in (57), (59), and (53) and the quad-pol Pauli components R_{SB}, R_{DB}, and R_{HV}

$$R_{SB} = \frac{|S_{SB}|_{PQ}}{|S_{SB}|} \tag{71}$$

$$R_{DB} = \frac{|S_{DB}|_{PQ}}{|S_{DB}|} \tag{72}$$

$$R_{HV} = \frac{|S_{HV}|_{PQ}}{|S_{HV}|}\ . \tag{73}$$

We selected some subset areas A1, A2, A3, and A4, which are shown in Fig. 5(a). Area A1 is over the sea. Using Google Earth we see that A4 is over forest and A2 is over residential houses aligned in azimuth direction. A3 is over residential houses which are not parallel to azimuth direction. A2 has much red color and therefore much double bounce scattering. A3 has much HV scattering. There are also many trees in the residential areas. We selected the same subset areas in Fig. 5(b) as in Fig. 5(a). Then, we estimated mean values of the Pauli components in (71)–(73) and then estimated the ratios. The results are shown in Table II. Both the ratios and amplitudes of the Pauli components are shown. The single bounce ratio R_{SB} varies from 1.09–1.14 in the different areas, the double bounce ratio R_{DB} varies from 0.71–0.88 and the HV ratio varies from 1.17–3.81. Hence, the pseudo single bounce $|S_{SB}|_{PQ}$ component is best reconstructed since the single bounce ratio R_{SB} is quite close to 1. R_{SB} is 1.09 over sea in A1 and 1.09 over forest in A4. In area A2 the double bounce ratio R_{DB} is 0.73 and, therefore, underestimated. The HV ratio R_{HV} is 3.81 and quite much overestimated. In area A3, where the houses are not aligned in azimuth direction, the reconstruction is better, the HV ratio R_{HV} is 1.17 and R_{DB} is 0.88. The ratios for the whole scene is 1.10, 0.80, and 1.36 for R_{SB}, R_{DB}, and R_{HV}, respectively. R_{HV} has the highest ratio, which explains that the green color dominates the image. The same trend was observed in [7].

From the analysis abovementioned, we can conclude the pseudo HV component is generally overestimated. The pseudodouble bounce component in some residential areas and also urban areas is underestimated, which may be caused by the assumption of reflection symmetry ([6]) mentioned in Section VI-B.

We found in [17 Fig. 5.10] that simulation of the $\pi/4$-mode performed better than the CTLR mode, which they also found in [7 Fig. 5]. We can visualize the effects found above if we zoom the subimage in the white rectangle in Fig. 5(b). We remove the *HV* component and display only the double bounce scattering (red) and surface scattering (green) components for quad-pol mode in Fig. 6(a) and for CTLR simulation in Fig. 6(b). The green color is almost the same in both images, which means that the surface scattering is quite well reconstructed with the CTLR simulation. It is obvious that the red color is more absent in Fig. 6(b) while some of the double bounce scattering (red) in Fig. 6(a) appears with approximately the same strength for double bounce and surface scattering (yellow) in Fig. 6(b).

B. Estimation of Pauli Components in RCM Compact Polarimetry Images

Fig. 7(a) shows an RG color composite of the *CH* and *CV* in the compact polarization option in a very high resolution beam mode (3 m) from RCM-1 over the city of Winnipeg in Canada. It is obvious that streets [see subset A3 in Fig. 7(a)], which are almost aligned in azimuth direction have much red color and is dominated by *CH* scattering. The streets, which are not aligned in azimuth direction have more yellow color, which means equal contribution from *CH* and *CV*. Many buildings and other infrastructure [lower part of Fig. 7(a)] have a strong yellow color, which means high backscatter of both *CH* and *CV*. The grass land and fields [see upper left part of Fig. 7(a) and subset A4 in Fig. 8(a)] have a more dark green color, which means mostly *CV* scattering, which is not very strong. In Fig. 7(b), we have estimated double bounce scattering S_{CDB} in (41) and single bounce scattering S_{CSB} in (42) and displayed the RG color composite. The grass land and fields are dominated by green color which means surface scattering. Also the Red River of the North going from the top to the bottom of the image as well as the Red River Floodway in the upper right of the image appear with green color. This indicates that wind may generate some ripples on the water surface.

Fig. 8 shows more detailed images from the rectangle in Fig. 7(a) and corresponding area in Fig. 7(b). The green color, which indicates surface scattering on the river is better visible in Fig. 8(b). The most striking red color in Fig. 7(a) is in the upper right part of the image and is enlarged in Fig. 8(a)(area A2). The high CH backscatter is due to several cemeteries with tombstones aligned very precisely in azimuth direction. The rows of tombstones are also well visible in Fig. 8(b) with double

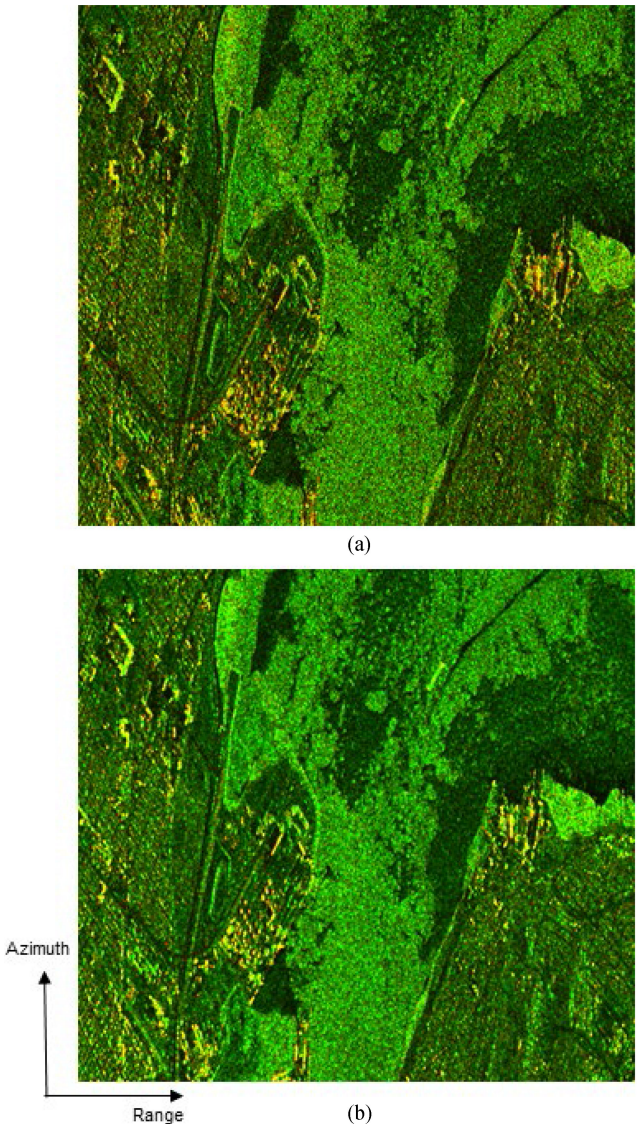

Fig. 6. RG color composite of double bounce (R) and surface (G) components within the rectangle shown in Fig. 5(b). Azimuth pixel spacing = 3.3 m and ground range pixel spacing = 3.1 m. (a) Quad-pol image in Fig. 5(a). (b) Simulated CTLR image in Fig. 5(b).

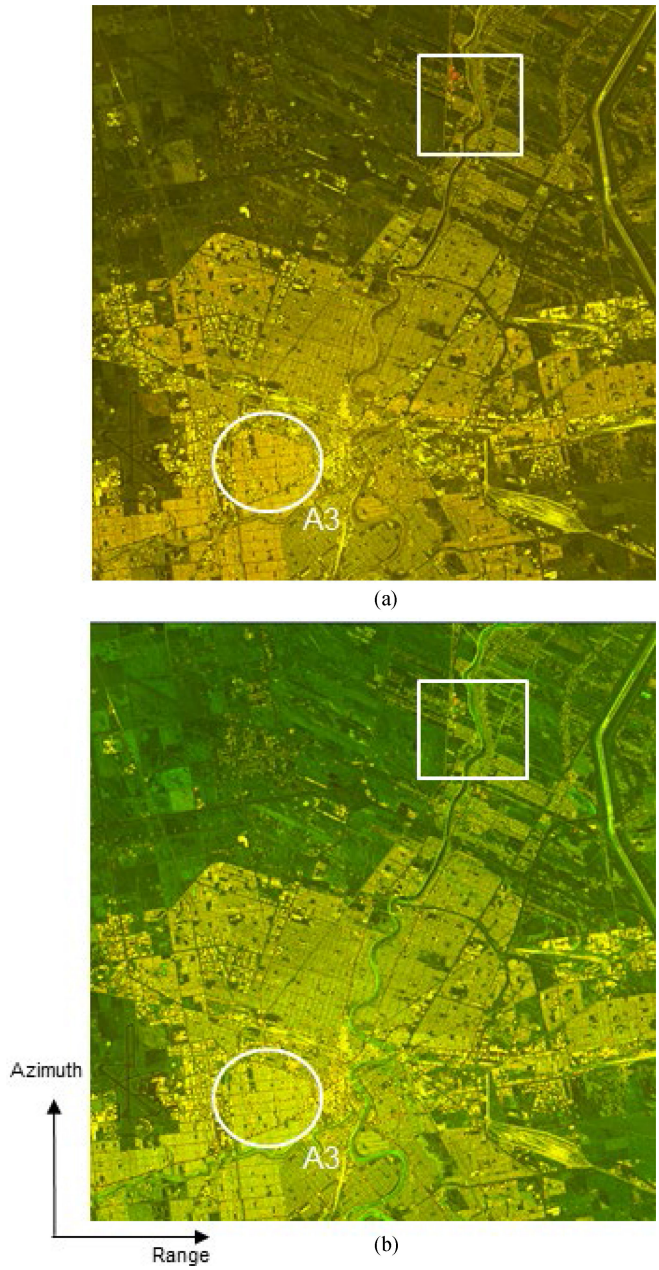

Fig. 7. Averaged 12 × 12 RCM-1 image of the second scene in Table I, very high resolution 3 m. The subset in the area A3 is used for estimation of the ratios R_{CHV} and R_{CSD} in (74) and (75). (a) RG color composite of *CH* (R) and *CV* (G). The area in the rectangle is shown in Fig. 8(a). (b) RG color composite of double bounce (R) and surface scattering (G). The area in the rectangle is shown in Fig. 8(b).

bounce scattering, however, also considerable amount of surface scattering.

Now, we do a more quantative analysis in Figs. 7 and 8. We define the ratio R_{CHV} of the absolute values of the *CH* and *CV* components

$$R_{\mathrm{CHV}} = \frac{|S_{CH}|}{|S_{CV}|} \tag{74}$$

and the ratio R_{CSD} of the absolute values of single bounce scattering S_{CSB} and the double bounce scattering S_{CDB}

$$R_{\mathrm{CSD}} = \frac{|S_{\mathrm{CSB}}|}{|S_{\mathrm{CDB}}|} \,. \tag{75}$$

We selected some subset areas A1, A2, and A4 in Fig. 8(a) and A3 in Fig. 7(b). Area A1 is over the Red River of the North and A4 is over fields. A2 is over the rows of tombstones and area A3 is over residential houses lying along streets, which are not parallel to azimuth direction. There are also many trees in the residential areas. We estimated mean values of the *CH, CV*, CSB, and CDB components in (74) and (75) in different areas and then estimated the ratios. The results are shown in Table III. For the whole scene the ratio R_{CHV} of the *CH* and *CV* is 1.09, quite close to 1, while the ratio R_{CSD} of CSB and CDB is 1.27 if we assume that the $\pi/2$ phase in (38) was cancelled in the receiver in the dataset we used. If we do not do that assumption, the ratio R_{CSD} is 1.02, hence, the double bounce and surface scattering are

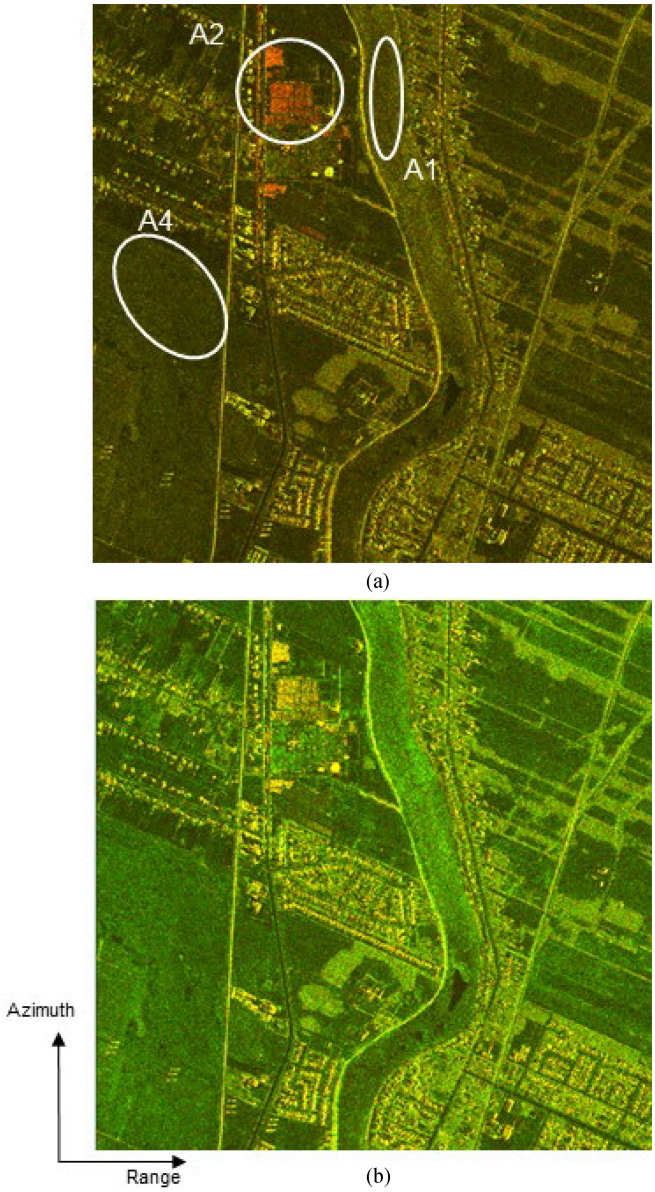

Fig. 8. (a) RG color composite of *CH* (R) and *CV* (G) averaged 2 × 2 in the area in the rectangle in Fig. 7(a). The subset areas A1, A2, and A4 and corresponding areas in Fig. 8(b) are used for estimation of the ratios R_{CHV} and R_{CSD}. (b) RG color composite of double bounce (R) and surface scattering (G) averaged 2 × 2 in the area in the rectangle in Fig. 7(b).

mostly equal. Since much of the image is over urban areas there is more double bounce scattering than single bounce scattering. The ratio R_{CHV} over the river in A1 and the fields in A4 are close to 1, hence, the amplitude in the two channels is almost the same. The ratio R_{CSD} is 1.72 over the river in A1 and 1.88 in A4 over the fields. This is an important finding, because it tells that surface on the river and the fields is dominated by single bounce scattering. Figs. 7(b) and 8(b) show that it is possible to extract double bounce and surface scattering from *CH* and *CV* channels in RCM images. However, to compare the quality of the extracted double bounce and single bounce scattering from RCM CP mode we should have quad-pol data over the same region, which was not available to us.

TABLE III
AMPLITUDES OF *CH* AND *CV* COMPONENTS IN FIGS. 7(A) AND 8(A) AND THEIR RATIOS R_{CHV}. AMPLITUDES OF SINGLE BOUNCE AND DOUBLE BOUNCE COMPONENTS IN FIGS. 7(B) AND 8(B) AND THEIR RATIOS R_{CDB}

	Full scene	A1	A2	A3	A4
R_{CHV}	1.09	1.08	2.42	1.18	0.98
$\lvert S_{CH}\rvert$	304	267	694	480	200
$\lvert S_{CV}\rvert$	279	247	287	401	204
R_{CSD}	1.27	1.71	0.82	1.04	1.83
$\lvert S_{CSB}\rvert$	454	436	679	749	353
$\lvert S_{CDB}\rvert$	358	254	831	719	193

The subset areas A1, A2, A3, and A4 used for ratio estimation are the same in Figs. 7(b) and 8(b), as shown in Figs. 7(a) and 8(a).

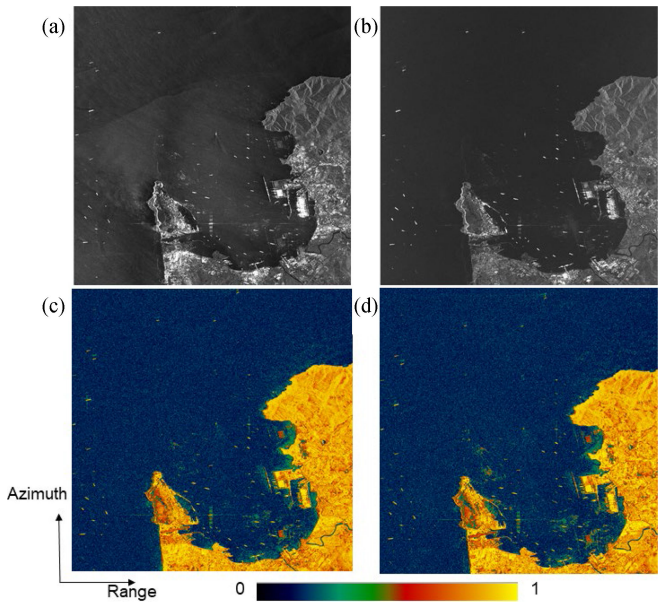

Fig. 9. Average 10 × 10 pixels. Gibraltar harbor. (a) Amplitude image of *HH* of TSX. (b) Amplitude image of *HV* of TSX. (c) Coherence of *HH* from TDX/TSX. (d) Coherence of *VV* from TSX/TDX.

C. Coherence Estimation in Bistatic TanDEM-X Images Using the Pauli Components

The third scene in Table I is over Gibraltar and shows the harbour and a lot of ships. The height of ambiguity is 111.5 m and the maximum coherence is quite close to 1. The full TSX scene in Table I has 23576 azimuth lines and 10192 range pixels. The azimuth resolution is 6.60 m and the slant range resolution is 1.18 m. Fig. 9(a) and (b) shows a 10 × 10 averaged subimage with 2500 × 2500 amplitude pixels from the HH and HV channels, respectively. The averaged azimuth pixel spacing is 22.2 m and the averaged slant range pixel spacing is 9.1 m. The TDX/TSX bistatic coherence images of *HH* and *VV* are shown in Fig. 9(c) and (d), respectively. Fig. 10(a) shows the Pauli decomposition of the TSX image. The sea appears blue and indicates mainly surface scattering. Buildings and infrastructure have mostly double bounce scattering (red). Land areas

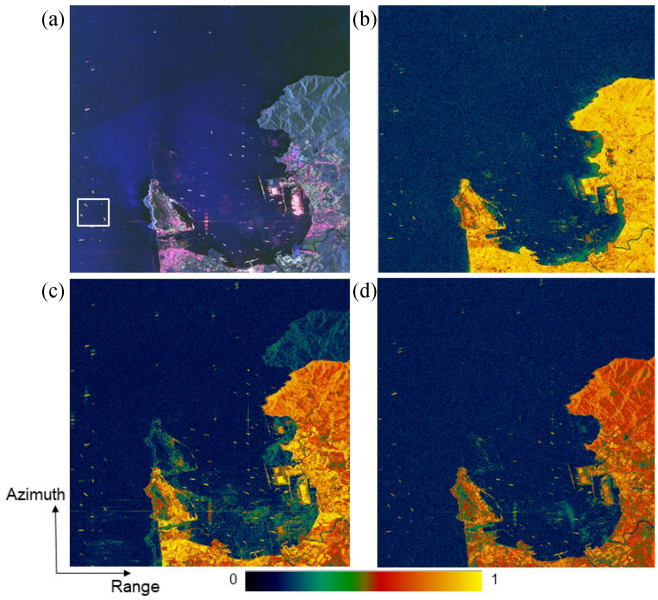

Fig. 10. Average 10 × 10 pixels. Gibraltar harbor. (a) RGB color composite of Pauli decomposition (B = surface, R = double bounce, G = |*HV*|) of TSX. (b) Coherence of surface scattering image of TSX/TDX. The white rectangle in (a) shows the area in Figs. 11 and 12. (c) Coherence of double bounce scattering image of TSX/TDX. (d) Coherence of the cross-polarization scattering image of TSX/TDX.

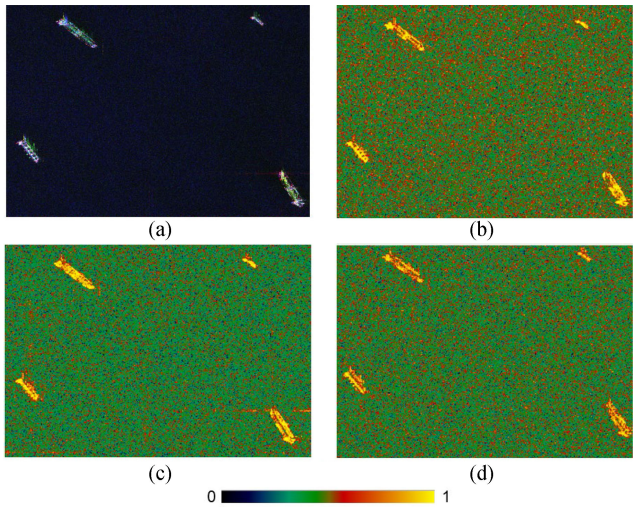

Fig. 11. Average 4 × 4 pixels. (a) RGB color composite for Pauli decomposition for TSX image (B = surface, R = double bounce, G = |*HV*|). (b) Coherence of surface scattering. (c) Coherence of double bounce scattering. (d) Coherence of cross-polarization scattering.

appear blue and green, a mix of surface, and cross-polarization scattering. We estimate the complex single bounce of the TSX SLC image, $S_{1_{SB}}$ in (62), and then the complex single bounce of the TDX image, $S_{2_{SB}}$ in (63). Then, the coherence of $S_{1_{SB}}$ and $S_{2_{SB}}$ is generated by estimating the complex average in windows with size n x n pixels. We estimate the double bounce images from TSX and TDX using (60) and (61), and then take the coherence in Fig. 10(c). The same is done for the HV images in Fig. 10(d). The number of complex pixels averaged in generation of the coherence images is 10 × 10 pixels in Fig. 10(b)–(d). In Fig. 10(a), the average is taken over the amplitudes.

The along-track distance between TSX and TDX is 201 m, which is enough to decorrelate the coherence on the sea surface, however, the coherence on moving ships is still quite high. We have studied two other TSX/TDX image pairs with along-track distances 173 m and 3 m (handwritten notes only). In the first case the coherence on the sea is considerably higher than the image pair with along-track distance 201 m. The coherence on the sea in the image pair with along-track distance 3 m is comparable with the coherence on land. This means that when the along-track baseline decreases, the coherence on the sea increases and makes detection of ships more difficult. If we compare the Pauli image in Fig 10(a) or the *HH* and *VV* images in Fig. 9(a) and (b) with the coherence images visually, it is clear that the ships are best detected in the double bounce image in Fig. 10(c). This is also the case when we compare Fig. 10(c) with the *HH* coherence and *VV* coherence in Fig. 9(c) and (d). Most of the ships in the upper part of the images are moving since they have visible wakes in the SAR images. Some of the ships are weaker in Fig. 10(b) and (d). The coherence in the surface scattering image is high in all land areas and higher than in the double bounce and cross-polarization image. Where the Pauli image in Fig. 10(a) shows double bounce (red color) the coherence is best in the double bounce coherence image Fig. 10(c). We also observe that the ghost images (azimuth ambiguities) of land areas are most dominating in the double bounce image. This is because the double bounce scattering is low over ocean areas.

In Fig. 11, four ships in the lower left corner of Fig. 10 are displayed in more detail and averaged 4 × 4 (see rectangle in Fig. 10(a)). The averaged azimuth pixel spacing is 8.9 m and the averaged slant range pixel spacing is 3.6 m. In Fig. 10(a), a weak wake is behind the three largest ships. The image in Fig. 11(a) is scaled lower to better see the colors of the ship pixels. Since the coherence in Fig. 11 is averaged 4 × 4 pixels and 10 × 10 in Fig. 10(b)–(d), the distribution of the coherence is substantially broader in Fig. 11, hence, the color is more green than blue. The coherence values of the ship pixels in Fig. 11(b)–(d) are not very different, however, some differences in the structure is apparent. The coherences of the pixels in the double bounce image may be somewhat higher than in the surface and cross-polarization images. Taking the upper left ship as an example, the mean coherence of the whole ship is 0.77, 0.82, and 0.68 in Fig. 11(b), (c), and (d), respectively.

D. Coherence Optimization of Bistatic TDX/TSX Images Using the Pauli Components

The optimization algorithm for coherence described in Section V is now used on the SLC data that we used in Section VI-C (see the third scene in Table I). The optimal coherence values γ_1, γ_2, and γ_3 described in Section V are shown in Fig. 12(a), 12(b) and (c), respectively. The maximum coherence in Fig. 12(a) corresponds to the first eigenvalue and has intermediate high values over the ocean. All pixels in the ship targets have values close to one. The minimum coherence in Fig 12(c) shows minimal values over media like the ocean, which may be to some extent

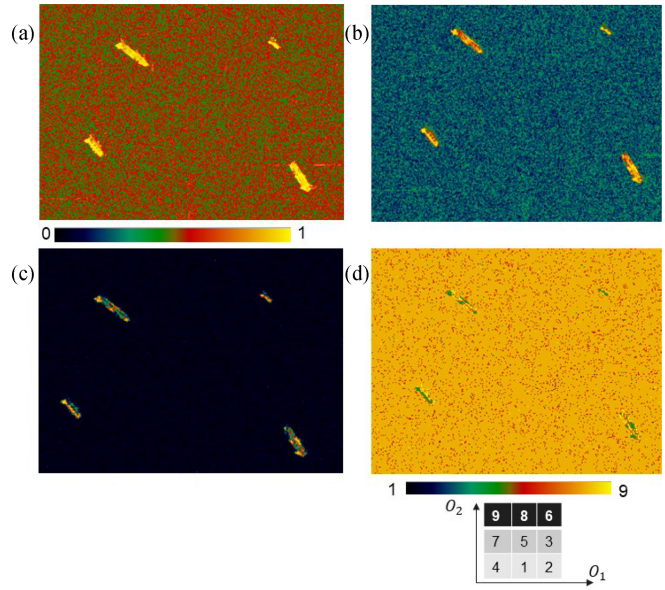

Fig. 12. (a) Optimal coherence γ_{opt_1}. (b) Optimal coherence γ_{opt_2}. (c) Optimal coherence γ_{opt_3}. (d) Discrimination of different optimal coherence set using O_1 and O_2.

decorrelated, however, the ships still get quite high values, some pixels close to one. Now, we want to classify different parts of the image. We remember the optimal coherences γ_{opt_1}, γ_{opt_2}, and γ_{opt_3} (positive values) in Section V and define the relative optimal coherences $\tilde{\gamma}_{opt\_i}$ as they did in [14] (see pp. 315–317)

$$\tilde{\gamma}_{opt\_i} = \frac{\gamma_{opt\_i}}{\sum_{j=1}^{3} \gamma_{opt\_j}} \quad \text{for } i = 1, 2, 3 \tag{76}$$

and two parameters O_1 and O_2 , which characterize the relative optimal coherence spectrum

$$O_1 = \frac{\tilde{\gamma}_{opt\_1} - \tilde{\gamma}_{opt\_2}}{\gamma_{opt\_1}} \tag{77}$$

$$O_2 = \frac{\tilde{\gamma}_{opt\_1} - \tilde{\gamma}_{opt\_3}}{\gamma_{opt\_1}} \,. \tag{78}$$

In Fig. 12(d), the parameters abovementioned are used to discriminate different optimal coherence values. The parameters given by (77) and (78) indicate relative amplitude variations between optimal coherencies. The classification is divided into nine classes by using O_1 and O_2. We can see that the ships have mostly green color, which means zone 4. For zone 4, we can see from Fig. 12(d) and (77) and (78) that O_1 and O_2 are both small, which means that the difference between the optimal coherences are both small. It can be seen in Fig. 12(c) that even for the third optimal coherence, there are coherence values close to 1. Some pixels in the ship belongs to zone 9, which means that the difference O_2 in (78) is large and the difference O_1 in (77) is small. The ocean is mainly orange, which means zone 8 with some noise from zone 7. In zone 8, O_2 is large and O_1 in the middle. Hence, the ships and the ocean surface have distinctive different properties. Since the ships may be moving, these results are solely dependent on the properties of the high TSX/TDX coherence due to the small time separation of TSX and TDX. Furthermore, the optimization algorithm utilizes the fact that the input polarimetric data is the Pauli components containing physical properties like double bounce, single bounce and cross-polarization scattering.

E. Some Final Comments on the Properties of the Pauli Decomposition

In the literature, there are a number of polarimetric decompositions including the Pauli decomposition [14]. Model-based decompositions, which are described in Freeman and Durden [18] and Yamaguchi *et al.* [19] used to calculate double bounce, surface, and volume scattering in terms of the scattering components S_{HH}, S_{HV}, and S_{VV}. The coherent Pauli decomposition components are simpler. The double bounce and single bounce components are not functions of S_{HV} and the cross-pol component is simply S_{HV}. However, the Pauli decomposition makes it possible to generate pseudodecompositions very simple from compact polarimetry. If the Yamaguchi decomposition should be generated from compact polarimetry data, it would be necessary to first reconstruct all pseudo quad-pol components. In this article, we derive the coherent Pauli decompositions using electrodynamic equations, which should be a supplement to the model-based decomposition in order to understand scattering mechanisms fully and comprehensively.

VII. Conclusion

In the literature, the components in the Pauli decomposition are usually derived from the scattering matrix. To get better insight in the reflection mechanisms we analysed the equations for reflection of polarized electromagnetic waves. We derived new formulas how the Pauli components can be extracted from simulated CTLR data using quad-pol data and from real compact polarized data. We used polarimetric data from RADARSAT constellation mission. We demonstrated how the unique quad-pol interferometric data from TSX and TDX could be used to estimate coherence of moving ships and how the coherence can be optimized and used for classification.

Acknowledgment

The author would like to thank the science team at DLR, T. Busche, and I. Hansjek at DLR for planning and delivery of CoSSC TanDEM-X data (AO-project NTI_INS6664), and also like to thank to the anonymous reviewers for giving valuable comments to the manuscript. RCM data could be freely downloaded from a Canadian government ftp site after a tip from the RCM mission manager at Canadian Space Agency, D. De Lisle.

References

[1] G. Kroupnik, D. De Lisle, S. Cote, M. Lapointe, C. Casgrain, and R. Fortier, "RADARSAT constellation mission overview and status," in *Proc. IEEE Radar Conf.*, Atlanta, GA, USA, 2021, pp. 1–5.

[2] S. Cote, M. Lapointe, D. De Lisle, E. Arsenault, and M. Wierus, "The RADARSAT constellation: Mission overview and status," in *Proc. EUSAR*, Leipzig, Germany, 2021, pp. 1–5.

[3] R. K. Raney, "Hybrid-polarity SAR architecture," *IEEE Trans. Geosci. Remote Sens.*, vol. 45, no. 11, pp. 3397–3404, Nov. 2007.

[4] R. K. Raney, "Hybrid dual-polarization synthetic aperture radar," *Remote Sens.*, vol. 11, no. 13. 2019. [Online]. Available: https://doi.org/10.3390/rs11131521
[5] J-C. Souyris, P. Imbo, R. Fjørtoft, S. Mingot, and J-S. Lee, "Compact polarimetry based on symmetry properties of geophysical media: The $\pi/4$ mode," *IEEE Trans. Geosci. Remote Sens.*, vol. 43, no. 3, pp. 634–646, Mar. 2005.
[6] M.J. Collins, M. Denbina, and G. Atteia, "On the reconstruction of quad-pol SAR data from compact polarimetry data for ocean target detection," *IEEE Trans. Geosci. Remote Sens.*, vol. 51, no. 1, pp. 591–600, Jan. 2013.
[7] M. E. Nord, T. L. Ainsworth, J.-S. Lee, and N. J.S. Stacy, "Comparison of compact polarimetric synthetic aperture radar modes," *IEEE Trans. Geosci. Remote Sens.*, vol. 47, no. 1, pp. 174–188, Jan. 2009.
[8] G. Krieger *et al.*, "TanDEM-X: A radar interferometer with two formation flying satellites," *Acta Astronatica*, vol. 89, pp. 1015–1027, 2016.
[9] K. Eldhuset, "Combination of stereo SAR and InSAR for DEM generation using TanDEM-X spotlight data," *Int. J. Remote Sens.*, vol. 38, no. 15, pp. 4362–4378, May 2017.
[10] K. Eldhuset, "Change detection using time and look angle series of geocoded TanDEM-X staring spotlight images," *IEEE J. Sel. Topics Appl. Earth Observ. Remote Sens.*, vol. 14, pp. 3824–3829, Mar. 2021.
[11] Government of Canada, "RADARSAT constellation mission. Access to RCM data," 2020. [Online]. Available: https://www.asc-csa.gc.ca/eng/satellites/radarsat/
[12] I. Hajnsek, T. Busche, G. Krieger, M. Zink, D. Schulze, and A. Moreira, "TanDEM-X Science Phase," 2014. [Online]. Available: https://tandemx-science.dlr.de
[13] U. Balss, H. Breit, S. Duque, T. Fritz, and C. Rossi, "TanDEM-X CoSSC generation and interferometric considerations," 2012. [Online]. Available: https://tandemx-science.dlr.de
[14] J-S. Lee and E. Pottier, *Polarimetric Radar Imaging: From Basics to Applications*. New York, USA: Taylor & Francis, 2009.
[15] D. Griffiths, *Introduction to Electrodynamics*. Cambridge, U.K.: Univ. Press, 2017.
[16] K.P. Papathanassiou, "Polarimetric SAR interferometry," Ph.D. dissertation, Dept. Phys., Techn. Univ. Graz, Graz, Austria, 1999.
[17] R.L. Lillestøl, K. Eldhuset, T.N. Hannevik, A.O. Knapskog, R.B. Olsen, and K.O. Viken, "Anvendelser av SAR-bilder fra satellitter over land," Tech. Rep. 19/01695, Norwegian Defence Res. Establishment, Kjeller, Norway, 2019. [Online]. Available: https://www.ffi.no/publikasjoner/arkiv/anvendelser-av-sar-bilder-fra-satellitter-over-land
[18] A. Freeman and S.L. Durden, "A three-component scattering model for polarimetric SAR data," *IEEE Trans. Geosci. Remote Sens.*, vol. 36, no. 3, pp. 936–973, May 1998.
[19] Y. Yamaguchi, A. Sato, W-M. Boerner, R. Sato, and H. Yamada, "Four-component scattering power decomposition with rotation of coherency matrix," *IEEE Trans. Geosci. Remote Sens.*, vol. 49, no. 6, pp. 2251–2258, Jun. 2011.

Knut Eldhuset was born in 1958. He received the M.Sc. (cand. scient.) degree in nuclear physics from the University of Oslo, Oslo, Norway, in 1983, and the Ph.D. (dr. scient.) degree in physics/signal processing from the University of Tromsø, Tromsø, Norway, in 1987.

He has been with the Norwegian Defence Research Establishment (FFI) since 1983, working on processing and applications of satellite Synthetic Aperture Radar (SAR) data. His research interests include a wide range of topics, including orbit simulation, geolocation, automatic ship detection, SAR/scanSAR processing, InSAR processing, scattering theory, polarimetry, MTI simulations, and processing of bistatic SAR data.

Dr. Eldhuset results have contributed to numerous national projects, to European defence research projects and to several studies for the European Space Agency. He has developed advanced algorithms for ship and wake detection, and for SAR processing using the Extended Exact Transfer Function, both of which were developed into commercial products by the Kongsberg Group. The latest SAR processing algorithm is the Decomposed Transfer Function. While his early work was focused on ERS, ENVISAT, and Radarsat-1, his more recent work has focused on polarimetric analysis of Radarsat-2 images and InSAR combined with stereoSAR using TerraSAR-X/TanDEM-X and COSMO-SkyMed for DEM generation and change detection.